2 **Forecasting and Identifying the Meteorological and Hydrological Conditions Favoring the**
3 **Occurrence of Severe Hazes in Beijing and Shanghai using Deep Learning**
4
5
6 Chien Wang
7
8 Laboratoire d'Aerologie, CNRS and University Paul Sabatier
9 14 Avenue Edouard Belin, 31400 Toulouse, France
10
11
12
13 March 2021; Revised August 2021
14
15
16
17
18
19
20
21
22 *Correspondence to*: Chien Wang (chien.wang@aero.obs-mip.fr)
23
24

Abstract. Severe haze or low visibility event caused by abundant atmospheric aerosols has become a serious environmental issue in many countries. A framework based on deep convolutional neural networks ~~containing more than 20 million parameters, namely HazeNet,~~ has been developed to forecast the occurrence of such events in two Asian megacities: Beijing and Shanghai. Trained using time sequential regional maps of up to 16 meteorological and hydrological variables alongside surface visibility data over the past 41 years, the machine has achieved a good overall ~~accuracy~~ performance in ~~associating~~ identifying the haze versus non-haze events ~~with~~ and thus their respectively favorite meteorological and hydrological conditions, with a validation accuracy of 80% in both Beijing and Shanghai cases, exceeding the frequency of non-haze events or no-skill forecasting accuracy, and a F1 score specifically for haze events nearly 0.5. Its performance is clearly better during months with high haze frequency, that is all months except dusty April and May in Beijing and from late autumn through entire winter in Shanghai. Certain valuable knowledge has also obtained from the training such as the sensitivity of the machine's performance to the spatial scale of feature patterns that could benefit future applications using meteorological and hydrological data. Furthermore, an unsupervised cluster analysis using features with a greatly reduced dimensionality produced by the trained ~~machine~~ HazeNet has, arguably for the first time, successfully categorized typical regional meteorological-hydrological regimes alongside local quantities respectively associated with haze and non-haze events in the two targeted cities, providing substantial insights to advance our understandings of this environmental extreme. Interesting similarities in associated weather and hydrological regimes between haze and false alarm clusters, or differences between haze and missing forecasting clusters have also been revealed, implying that factors such as energy consumption variations, long-range aerosol transport, and beyond could also influence the occurrence of hazes, even under unfavorite weather conditions.

1 Introduction

Frequent low visibility or haze events caused by elevated abundance of atmospheric aerosols due to fossil fuel and biomass burning have become a serious environmental issue in many Asian countries in recent decades, interrupting economic and societal activities and causing human health issues (*e.g.*, Chan and Yao, 2008; Silva et al., 2013; Lee *et al*., 2017). For example, rapid economic development and urbanization in China have caused various pollution-related health issues particularly in populated metropolitans such as Beijing-Tianjin region and Yangtze River delta centered in Shanghai (*e.g.*, Liu *et al*., 2017). In Singapore, the total economic cost brought by severe hazes in 2015 is estimated to be $510 million (0.17% of the GDP), or $643.5 million based on a wiling-to-pay analysis (Lin *et al*., 2016). To ultimately prevent this detrimental environmental extreme from happening requires rigid emission control measures in place through significant changes in energy consumption as well as land and plantation management. Before all these measures could finally take place, it would be more practical to develop skills to accurately predict the occurrence of hazes hence to allow mitigation measures to be implemented ahead of time.

Severe haze events arise from the solar radiation extinction by aerosols in the atmosphere, this mechanism can be enhanced with the increase of relative humidity that enlarges the size of particles (*e.g.*, Kiehl and Briegleb 1993). Aerosols also need favorite atmospheric transport and mixing conditions to reach places away from their immediate source locations, while their lifetime in the atmosphere can be significantly reduced by rainfall removal. In addition, soil

69 moisture is also a key to dust emissions. Therefore, meteorological and hydrological conditions
70 are critical to the occurrence of haze events besides particulate emissions. To forecast the
71 occurrence of such events using existing atmospheric numerical models developed based on fluid
72 dynamics and explicit or parameterized representations of physical and chemical processes, the
73 actual task is to accurately predict the concentration of aerosols at a given geographic location
74 and a given time in order to correctly derive surface visibility (*e.g.*, Lee *et al.* 2017 & 2018).
75 However, the propagation of numerical or parameterization errors through the model integration
76 could easily drift the model away from the original track, not mentioning that lack of real-time
77 emission data alone would simply handicap such an attempt. Therefore, a more fundamental
78 issue in practice is whether these models could reproduce the *a posteriori* distribution of the
79 possible outcomes of the targeted low-probability extreme events. Ultimately, lack of knowledge
80 about the extreme events would, in turn, hinder the effort to improve the forecasting skills.
81   Differing from the deterministic models, an alternative statistical prediction approach could
82 be adopted, if the predictors of a targeted event could be identified and a statistical correlation
83 between them could be established with confidence. However, this is a rather difficult task for
84 the traditional approaches, because it requires an analysis dealing with a very large quantity of
85 high-dimensional data to establish a likely multi-variate and nonlinear correlation that can be
86 generalized. Nevertheless, such attempts can obviously benefit now from the fast-growing
87 machine learning (ML) and deep learning (DL) algorithm development (*e.g.*, LeCun *et al.*,
88 2015). In addition, technological advancement and continuous investment from governments and
89 other sectors across the world have led to a rapid increase of quantity alongside substantially
90 improved quality of meteorological, oceanic, hydrological, land, and atmospheric composition
91 data. These data might still not be sufficient for evaluating and improving certain detailed
92 aspects of the deterministic forecasting models. However, rich information contained in these
93 data about favorite environmental conditions for the occurrence of extreme events such as hazes
94 could already have a great value for developing alternative forecasting skills.
95   Many Earth science applications dealing with meteorological or hydrological data need a
96 trained machine to not only forecast values but also recognize patterns or images. However, this
97 can easily lead to a curse of dimensionality of many traditional ML algorithms. Fortunately, deep
98 learning that directly links large quantity of raw data with targeted outcomes through deep
99 convolutional neural networks or CNNs (Goodfellow *et al.*, 2016) offers a clear advantage in
100 sufficiently training deep networks suitable for solving highly nonlinear issues. In doing so, DL
101 can also eliminate the possible mistakes in data derivation or selection introduced by subjective
102 human opinion regarding a poorly understood phenomenon. Recently, DL algorithms have been
103 explored in various applications in atmospheric, climate, and environmental sciences, ranging
104 from recognizing specific weather patterns (*e.g.*, Liu *et al.*, 2016; Kurth *et al.*, 2018; Lagerquist
105 *et al.*, 2019; Chattopadhyay *et al.*, 2020), weather forecasting including hailstorm detection (*e.g.*,
106 Grover *et al.*, 2015; Shi *et al.*, 2015; Gagne *et al.*, 2019), to deriving model parameterizations
107 (*e.g.*, Jiang *et al.*, 2018), and beyond.
108   In certain applications, the targeted outcomes are the same features as the input but at a
109 different time, *e.g.*, a given weather feature(s) such as temperature or pressure at a given level.
110 The forecasting can thus be proceeded by using pattern-to-pattern correlation from a sequential
111 training dataset with spatial-information-preserving full CNNs such as U-net (Ronneberger *et al.*,
112 2015; Weyn *et al.*, 2020). However, this is certainly not the case for the applications where the
113 environmental conditions associated with targeted outcome are yet known. For such applications,
114 a possible solution is to utilize a large quantity of raw data with minimized human intervention in

115 data selection to train a deep CNN to associate targeted outcomes with favorite environmental
116 conditions. This study represents such an attempt, where a DL forecast framework is trained to
117 identify the meteorological and hydrological conditions associated with the occurrences of
118 severe hazes. The DL framework has been developed initially with the severe hazes in Singapore
119 (Wang, 2020), and now hazes in two megacities of China, Beijing and Shanghai. In terms of
120 particulate pollutant emissions, all these cities share certain sources including fossil fuel
121 combustions from transportation, domestic, and industries. On the other hand, each city also has
122 its own unique sources, for instance, desert and perhaps anthropogenic dust for Beijing, and
123 massive biomass burning in Singapore (Chen *et al.*, 2013; Liu *et al.*, 2017; Lee *et al.*, 2017,
124 2018, & 2019). It is obvious that besides meteorological and hydrological conditions, dynamical
125 patterns of anthropogenic activities leading to the emissions of particulate matters are also
126 important factors behind the occurrence of severe hazes. Nevertheless, the major purpose of this
127 study is to advance our fundamental knowledge about the weather conditions favoring the
128 occurrence of hazes and, through an in-depth analysis on the forecasting results to identify the
129 limit of such a machine and thus to provide useful information for establishing a more complete
130 forecasting platform for the task.
131   In the paper, the architecture alongside method and data for training are firstly described after
132 this introduction, followed by a discussion of training and validation results. Then, an
133 unsupervised cluster analysis benefited from the trained machine is introduced along with the
134 results that furthers the understanding of the CNN's performance and summarizes, for the first
135 time, the various typical meteorological and hydrological regimes associated with haze versus
136 non-haze situations in the two cities. The last section concludes the effort and major findings.

137 **2 Network Architecture, Training Methodology and Data**

138 **2.1 Network architecture**
139   The convolutional neural network used in this study, the HazeNet (Wang 2020), has been
140 developed by adopting the general architecture of the CNN developed by the Oxford
141 University's Visual Geometry Group or VGG-Net (Simonyan and Zisserman, 2015). The actual
142 structure alongside hyper-parameters of HazeNet have been adjusted and fine-tuned based on
143 numerous test trainings. In addition, certain techniques that were not available when the original
144 VGG net was developed, *e.g.*, batch normalization (Ioffe and Szegedy, 2015), have been
145 included as well. The current version for haze applications of Beijing and Shanghai, though
146 trained separately, contains the same number of parameters of 20,507,161 (11,376 non-trainable)
147 owing to the same optimized kernel sizes. Figure 1 shows the general architecture of a HazeNet
148 version with 12 convolutional and 4 dense layers (in total 57 layers).
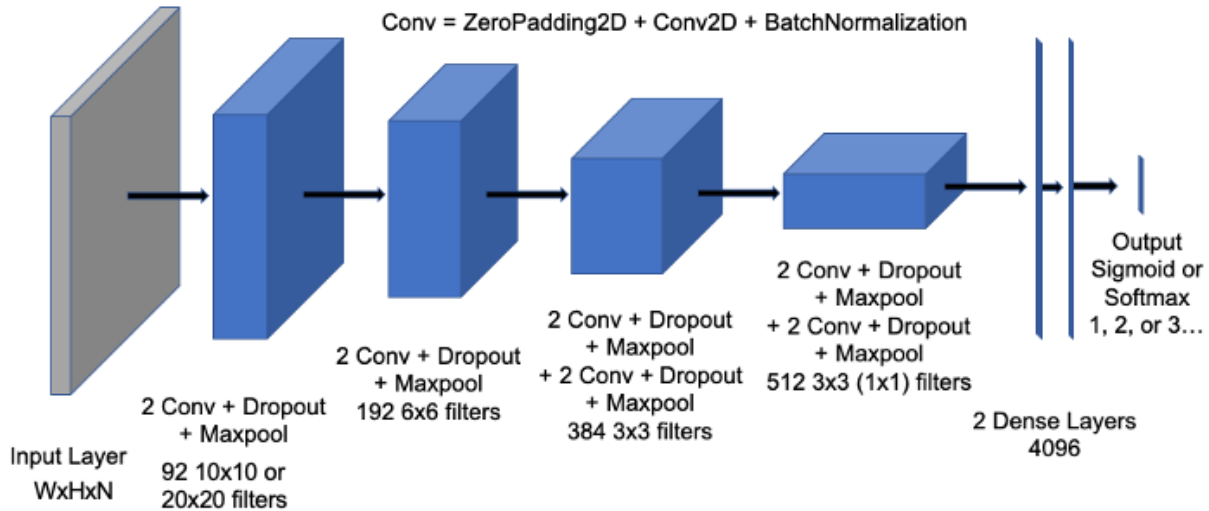
149
150 **Figure 1**. Architecture of the 12 convolutional plus 4 dense layer HazeNet. Here "Conv" represents a unit
151 containing a zero-padding then a 2D convolutional layer, followed by a batch normalization layer. There
152 is a flatten layer before the 2 dense layers. W = width, H = height, and N = number of features of the
153 input fields, they are 64, 96, and 16 for Beijing, and 64, 64, and 16 for Shanghai case, respectively.

154   The network has been trained in a standard supervised learning procedure for classification,
155 where the network takes input features to produce classification output that are then compared
156 with known results or labels based on observations. The coefficients of the network are thereafter
157 optimized in order to minimize the error between the prediction and the observation or label. The
158 loss function used in optimization is cross-entropy (*e.g.*, Goodfellow *et al*., 2017). Such a
159 procedure is repeated until the performance of the network can no longer be improved. In
160 practice, the trainings usually last about 2000 epochs (each epoch is a training cycle that uses up
161 the entire training dataset). This procedure in nature is to train a deep CNN to recognize then
162 associate input features (bundled meteorological and hydrological conditions in this case) with
163 corresponding class, *i.e.*, severe haze events or non-haze events. As a result, the knowledge
164 specifically about the favorite meteorological and hydrological conditions of severe hazes could
165 be advanced.
166
167 **2.2 Training data and methodology**
168   The labels for the training are derived using the observed daily surface visibility (*vis.*
169 thereafter), obtained from the Global Surface Summary Of the Day or GSOD dataset consisting
170 of daily observations of meteorological conditions from tens of thousands of airports around the
171 globe (Smith *et al*., 2011). In the cases of Beijing and Shanghai, data are from observations in
172 corresponding airports of these two cities during the time from 1979 to 2019, containing 14,975
173 samples. For simplicity, the discussions will be mainly on the 2-class training, where events with
174 *vis.* ≤ the long-term mean value of the 25th percentile or p25 of *vis.* (6.27 km in Beijing, 5.95 km
175 in Shanghai; Fig. 2, right panel; also Fig. S1 in Supplementary) are defined as class 1 or severe
176 hazes, otherwise the class 0 or non-haze cases. Although p25 values vary interannually, their
177 long-term means actually represent a substantial reduction of *vis.* due to high particulate
178 pollution (*e.g.*, Lee *et al*., 2017). Note that unlike in the case of Singapore (Wang 2020), fog and
179 mist are more common low visibility events in Beijing and Shanghai and thus have been

180 excluded from the labels of severe hazes by following GSOD fog marks. The number of severe
181 haze events occurred during 1979-2019 defined in the above procedure is 3099 and 2099 for
182 Beijing and Shanghai, or in a frequency of 20.7% and 20.0%, respectively.
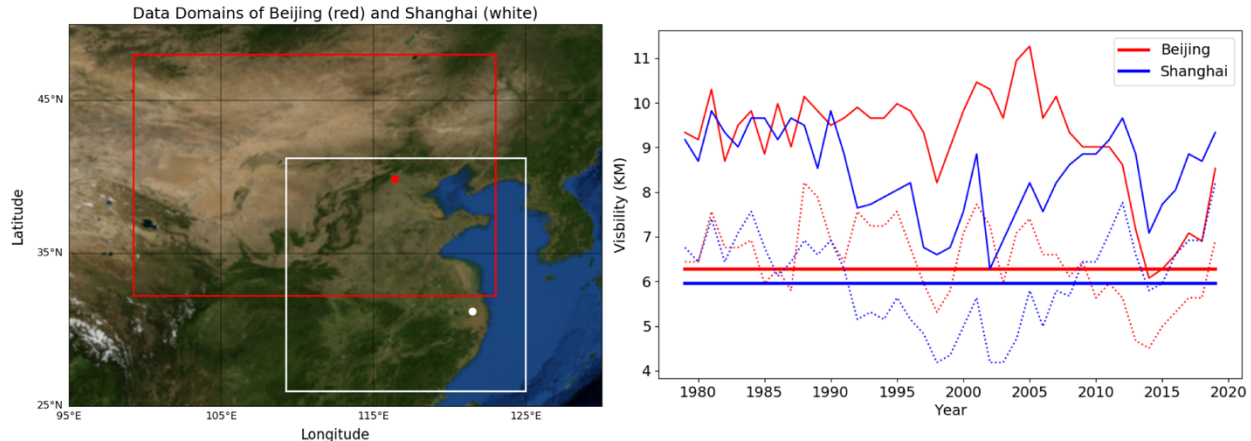
183
184 **Figure 2**. (Left) The input-feature defining domains for Beijing (red box and dot, 99.25 - 123E, 32.25-
185 48N; 96x64 grids with ERA5 data) and Shanghai (white box and dot, 109.25-125E, 26-41.25N; 64x64
186 grids), made using Basemap library, a matplotlib extension. (Right) Annual means (solid curves), 25th
187 percentiles (dash curves), and 25th percentile means (solid straight lines) of surface visibility in Beijing
188 (red) and Shanghai (blue) between 1979 and 2019.

189   The training and validation of HazeNet also need the input features with the same sample
190 dimension of the labels. These input data are derived from hourly maps of meteorological and
191 hydrological variables covering the data collection domain (Fig. 2, Left), obtained from ERA5
192 reanalysis data produced by the European Centre for Medium-range Weather Forecasts or
193 ECMWF (Hersbach *et al*., 2020). These data are distributed in a grid system with a horizontal
194 spatial interval of 0.25 degree. Up to 16 features are derived from the original hourly data fields
195 covering the analysis domain respectively for Beijing (64x96 grids) and Shanghai (64x64 grids),
196 including: daily mean of surface relative humidity (REL thereafter); diurnal change as well as
197 daily standard deviation of 2-meter temperature or DT2M and T2MS, respectively; daily mean of
198 10-meter zonal and meridional wind speed or U10 and V10, respectively; daily mean of total
199 column water (TCW); daily mean (TCV) and diurnal change (DTCV) of total column water
200 vapor; daily mean of planetary boundary layer height (BLH); daily mean soil water volume in
201 soil layer 1 and 2 or SW1 and SW2, respectively; daily mean of total cloud cover (TCC); daily
202 mean geopotential heights at 500 (Z500) and 850 (Z850) hPa pressure levels along with their
203 diurnal changes D500 and D850, respectively. All input features have been normalized into a
204 range of [-1, +1] (Fig. S2 in Supplementary).
205   Before the training, the entire samples of labels alongside corresponding input features were
206 randomly shuffled first then split as: 2/3 of the samples went to training set and 1/3 to validation
207 set, each is used duly for its designated purpose throughout the entire training process without
208 switch. The above procedure treats each of the events as an independent one. For the
209 convenience in comparing performance or restarting training based on a saved machine, a saved
210 training dataset alongside a holdout validation dataset that has never been used in training,
211 produced following the above procedure, was used.
212   The number of samples used in training HazeNet is rather limited in deep learning standard.
213 However, to associate 16 joint two-dimensional maps with targeted labels even with the current
214 number of samples is still a demanding task, requiring a deep CCN to accomplish. Furthermore,

215 targeted severe hazes are a low probability event. Its frequency of appearance is about 20.0% in
216 Beijing and Shanghai cases. Therefore, trained machine would easily bias toward the
217 overwhelming non-haze events. To resolve these issues, a combination of class-weight and batch
218 normalization has been implemented in HazeNet, both using corresponding Keras functions. The
219 class weight is to change the weight of training loss of each class, normally by increasing the
220 weight of the low frequency class. Class weight coefficient was calculated based on the ratio of
221 class 0 to class 1 frequency. Batch normalization (Ioffe and Szegedy, 2015) is an algorithm to
222 renormalize the input distribution at certain step (*e.g.*, each mini batch) to eliminate the shift of
223 such distribution during optimization. The above approach has effectively reduced the overfitting
224 while overcome the data imbalance issue, making the long training of a deep CNN become
225 possible (Wang, 2020). Entire trainings have been conducted using a NVIDIA Tesla V100-
226 SXM2 GPU cluster, costing 25s and 17s per epoch for the machine of Beijing and Shanghai,
227 respectively.

229 **2.3 Kernel size optimization.**
230 ~~Kernel size optimization.~~ As in the cases of other CNNs, there are many hyperparameters
231 need to be determined or optimized. These have been done through numerous testing trainings.
232 In practice, it occurs that, the deep architecture of HazeNet and the long training procedure have
233 actually made the performance less sensitive to many hyperparameters of the network. One
234 hyperparameter, however, is specifically interesting to explore for an application using large
235 quantity of meteorological maps, that is the kernel size of the first convolutional layer, where the
236 input data, *i.e.*, meteorological and hydrological maps are convoluted then propagated into the
237 subsequent layers. Meteorological maps or images often contain characteristic patterns with
238 different spatial scales. Intuitively, preserving these patterns could be important in predicting the
239 targeted extremes. Apparently, a larger kernel size produces smoother output images from the
240 first convolutional layer, while a smaller kernel size can preserve many spatial details of the
241 meteorological maps as demonstrated from the layer output shown in Fig. 3. In practice,
242 however, the patterns produced by the latter configuration might be too complicated for the
243 networks to recognize and to perform classification, whereas patterns resulted from a relatively
244 larger kernel size for the first convolutional layer might be more characteristic for the task. The
245 actual result suggests that HazeNet configured with a first-layer kernel size of 20 to 26 or close
246 to 5 – 6 degrees in spatial 'resolution', consistently produces a better performance (about a 10%
247 improvement in *F1 score*~~; see next section and Method~~) than that by a smaller kernel size of 3 or
248 6. As a result, a kernel size of 20 has been adopted as the default configuration for the first 2
249 convolutional layers in this study.

250
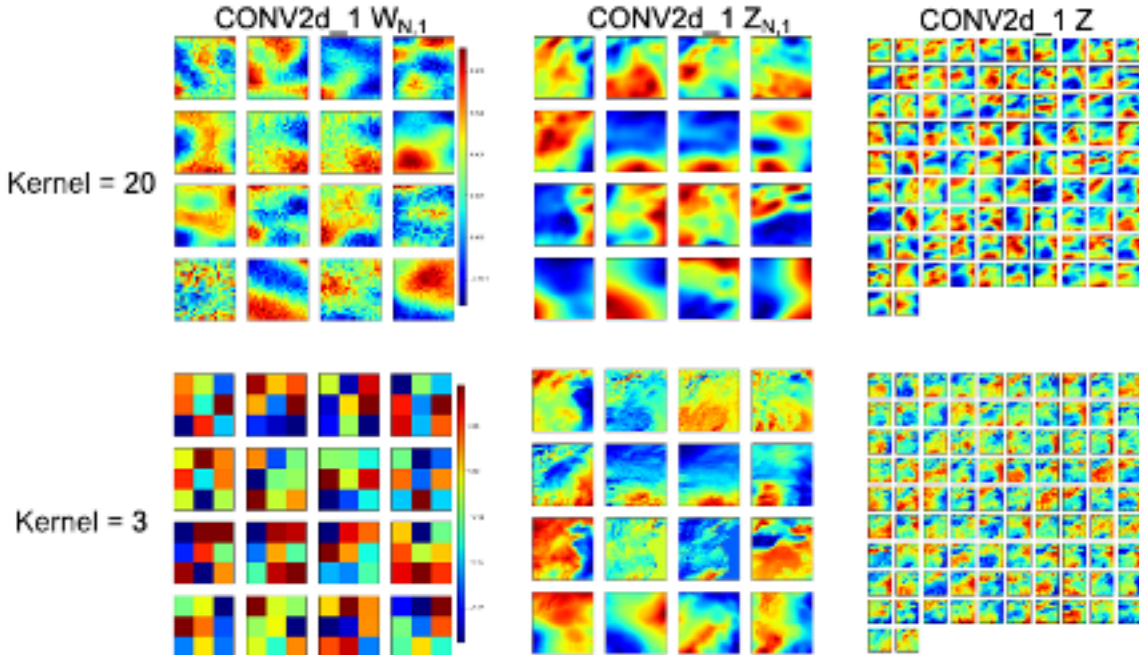
Figure 3. (Left column) Weight coefficients of the first filter set ($W_{N,1}$), (Middle column) partial output for each feature ($Z_{N,1}$), and (Right column) the output (Z) of the first convolution layer (CONV2d_1) with two selected kernel sizes or ks: (upper panels) 20x20 and (lower panels) 3x3. Here *W* represents the filters and *Z* the output of convolution, the subsets of Z before the feature dimension is merged can be expressed as: $Z_{N,i} = W_{N,i}(ks, ks) \cdot f_N^T(ks, ks)$, with the order of input features $N = 1,\dots 16$ and *i* represents the convolutional layer index, *i.e.*, 1 is the first layer or CONV2d_1. For the first layer, input feature size is $(h,w) = (64, 64)$, the sets of filters is 92, thus the final output $\bar{Z}$ has a dimension of (h-ks+1, w-ks+1, 92). Shown are results from the trainings for Shanghai haze cases.

3 Training and Validation Results of Haze Forecasting

Currently, it is still difficult to find any practical score in forecasting the occurrence of severe hazes for comparison. Therefore, the performance of HazeNet has been mainly measured by using certain commonly adopted metrics for classification largely derived from the concept of the so-called confusion matrix (*e.g.*, Swets, 1988; Table A), including *accuracy*, *precision*, *recall*, *F1 score*, *equitable threat score* or *ETS*, and *Heidke skill score* or *HSS* (Appendix A). Unless otherwise indicated, the discussions on the performance scores are hereafter referring to the severe haze class, or class 1, and obtained from validation rather than training. In all the cases, the performance metrics referring to non-haze or class 0 has much better scores. Also note that, unless otherwise indicated, results shown in this Section are obtained using 16 features.

269
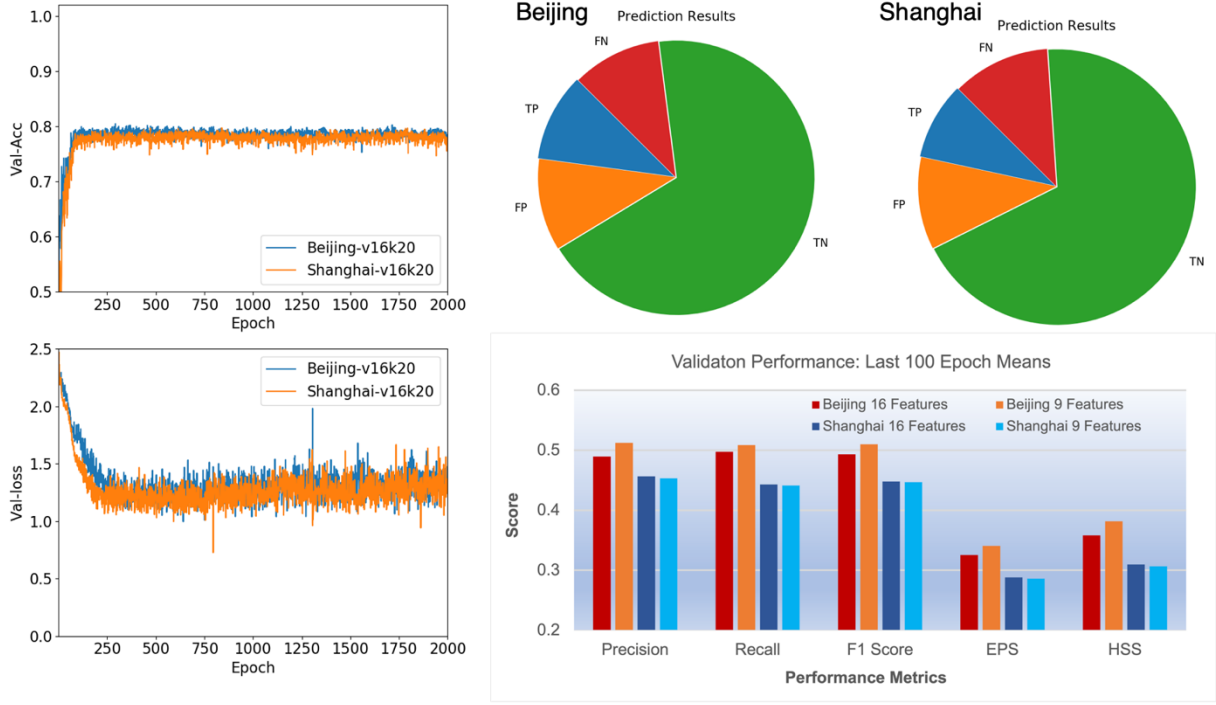
Figure 4. (Left) Validation accuracy (top panel) and loss (lower panel) of HazeNet with 16 features for Beijing and Shanghai cases, kernel size for the first filter is 20x20. (Right Top) Prediction outcomes in reference to haze events or class 1 of Beijing and Shanghai with 16 features. Here TP = true positive, TN = true negative, FP = false positive, and FN = false negative prediction outcomes. (Right Bottom) Scores of performance metrics as last 100 epoch means for Beijing and Shanghai with 16 and 9 features, respectively.

In order to train a stable machine, trainings with 2000 epochs or longer have been conducted instead of using certain commonly adopted skills such as early stop. As a result, the validation performance metrics of the trained machines all appeared to be stabilized by approaching the end of training (Fig. 4). These scores were consistent with the results of ensemble training with the same configuration but different randomly selected training and validation datasets, also comparable among trainings with different configurations. Overfitting has been clearly overcome due to such a long training procedure alongside the adoption of class weight and batch normalization. In a 2-class classification (haze *vs*. non-haze), trained deep HazeNet can always reach an almost perfect training accuracy (*e.g*., 0.9956 for Beijing cases) and a validation accuracy of 80% (frequency of non-haze events or no-skill forecasting accuracy) in both Beijing and Shanghai cases (Fig. 4, left). At the same time, the performance scores in predicting specifically severe hazes are also very reasonable, *e.g*., for Beijing cases either precision or recall exceeds 0.5 (they normally evolve in opposite direction), leading to a nearly 0.5 *F1 Score* (Fig.4, right). The corresponding scores in training are obviously much higher, *e.g*., with precision, recall, and F1 as 0.9804, 0.9980, and 0.9880, respectively for Beijing cases, owing to the deep and thus powerful CNNs. HazeNet performed slightly better than several known deep CNNs such as Inception Net V3 (Szegedy *et al*., 2015), ResNet50 (He *et al*., 2015), and VGG-19 (Simonyan and Zisserman, 2015) in the same haze forecasting task (Wang, 2020). Nevertheless, as indicated previously that a nearly perfect validation performance is not realistic since meteorological and hydrological conditions are not the only factors behind the occurrence of haze events.

298   Looking into the specific prediction outcomes in referring to severe haze, the trained machine
299 has produced considerably higher ratio of true positive or TP outcomes than in the Southeast
300 Asia cases (Wang, 2020) despite a number of outcomes of false positive or FP (*i.e.*, false alarm)
301 and false negative or FN (*i.e.*, missing forecast). In forecasting the severe hazes in Beijing, the
302 trained machine performs reasonably well throughout all months except for April and May or the
303 major dusty season there, producing F1 score, ETS, and HSS all exceed or near 0.5 as well as the
304 number of TP outcomes is higher than that of FN (Fig. 5). HazeNet actually performs better in
305 months with more observed haze events. For Beijing, the lowest haze season is during the dusty
306 April and May when all the major performance metrics are lower than 0.4, and the machine
307 produces more missing forecasts than true positive outcomes. The relatively poor performance in
308 spring suggests that the weather and hydrological features associated with dust-dominated haze
309 events during this period might differ from the situations in the other seasons when hazes are
310 mainly caused by local particulate pollution. For Shanghai cases, HazeNet performs better during
311 late autumn and entire winter (from November to February) when haze occurs most frequently
312 (not shown). The worst performance comes from the monsoon season (July to October), or the
313 season with lowest haze cases.
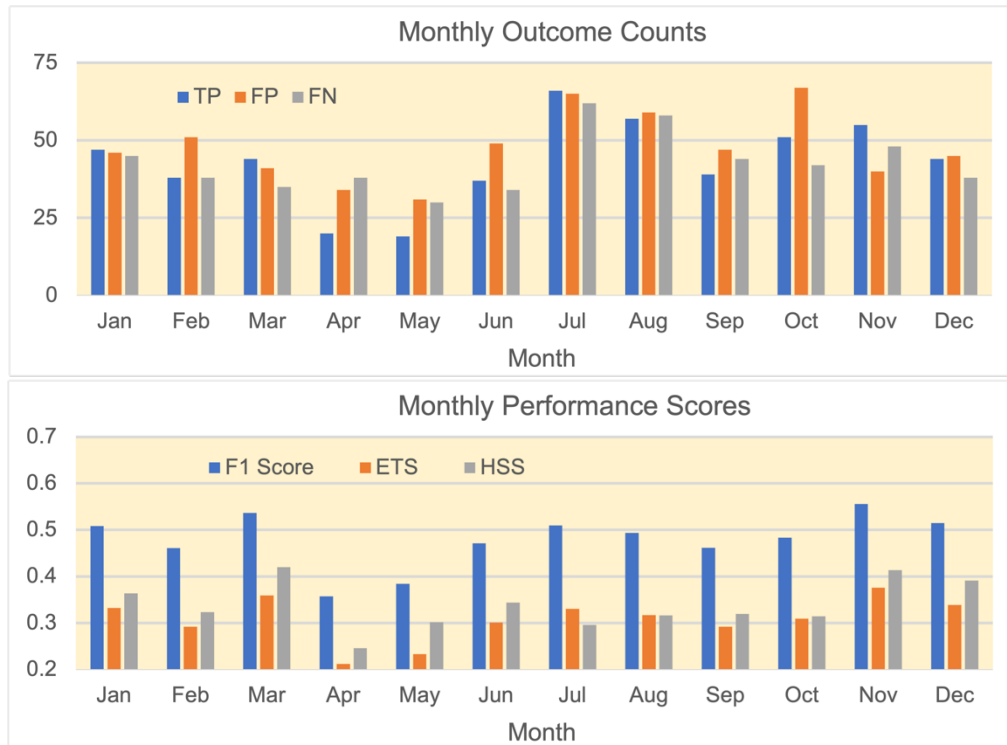
314

315
316 **Figure 5.** (Top) Monthly counts of predicted TP, FP, and FN outcomes and (Bottom) performance scores
317 for each month. All from validation of Beijing cases with 16 features.

318   **Reducing the number of input features**. One recognized advantage of deep CNN in
319 practice is its capacity to directly link the targeted outcome with a large quantity of raw data,
320 thus avoid human misjudgment in selecting and abstracting input features due to a lack of
321 knowledge about the application task. Nevertheless, for an application such as this one that uses
322 a large number of meteorological and hydrological variables (or channels in machine learning
323 term), reducing the number of input features with a minimized influence on the performance can
324 still benefit the efforts of establishing physical or dynamical causal relations and beyond.

325   There are certain available methods to rank features then reduce some unimportant ones.
326 These do not work straightforwardly for deep CNNs (*e.g.*, McGovern *et al*., 2019). In the
327 previous effort, this has been done by testing the sensitivity of the full network performance in
328 real training with either a single feature only or all but one features (Wang, 2020), which
329 apparently is also a demanding task. Here, another attempt has been made to use a trained then
330 saved machine to examine the sensitivity of the network to various features (Appendix B).
331   The sensitivity analyses using trained machines for Beijing and Shanghai have obtained
332 largely consistent results, indicating that the network is more sensitive to the same 9 features
333 than the other 7 (Fig. S3). The highest-ranking features though differ, with diurnal change of
334 column vapor (DTCV) and soil water content in the second soil layer (SW2) as the most
335 sensitive features for Beijing, while relative humidity (REL) and planetary boundary layer height
336 (BLH) for Shanghai. Most importantly, trainings using only the top 9 most sensitive features
337 have produced a performance equivalent to or even better than the same training but with 16
338 features (Fig. 4, Right Bottom). With reduced number of features, many further analyses can be
339 conducted with less workload and produce results that are easily understood.

340 **4 Identifying and Categorizing the Typical Regional Meteorological and Hydrological**
341 **Regimes Associated with Haze Events**

342   A major purpose of this study is to identify the meteorological and hydrological conditions
343 favoring the occurrence of severe hazes in the targeted cities. When using a dataset with a large
344 number of samples, this type of analyses could be better accomplished by applying, *e.g.*, cluster
345 analysis (*e.g.*, Steinhaus, 1957), a standard unsupervised ML algorithm that groups data samples
346 into various clusters in such a way that samples in the same cluster are more similar to each other
347 than to those in other clusters. Specifically for this study, the derived clusters would likely
348 represent various regimes in terms of combined meteorological and hydrological conditions for
349 associated events. However, applying cluster analysis directly to a large number of samples, each
350 with a feature volume of ~50000 is an uneasy task. A dimensionality reduction is apparently
351 needed to reduce the feature volume of data.
352   In practice, a trained CNN is actually an excellent tool for this purpose. It encodes
353 (downscales) the input with large feature volume into data with a much smaller size in the so-
354 called latent space (*i.e.*, the output of the layer before the output layer) while equal predictability
355 for the targeted events. This functionality of CNN has been used in developing various
356 generative DL algorithms from variational autoencoder or VAE to different generative
357 adversarial networks or GANs (*e.g.*, Forest, 2019). Therefore, the trained HazeNet for Beijing
358 and Shanghai using 9 instead of 16 features, benefited from the effort of reducing the number of
359 input features as described in the end of last Section, have been used in this study here to produce
360 data with reduced size suitable for clustering (Fig. 6; see also Appendix C). The new sample-
361 feature set with a size of 14,975×512 produced from this procedure was then used in cluster
362 analysis.
363
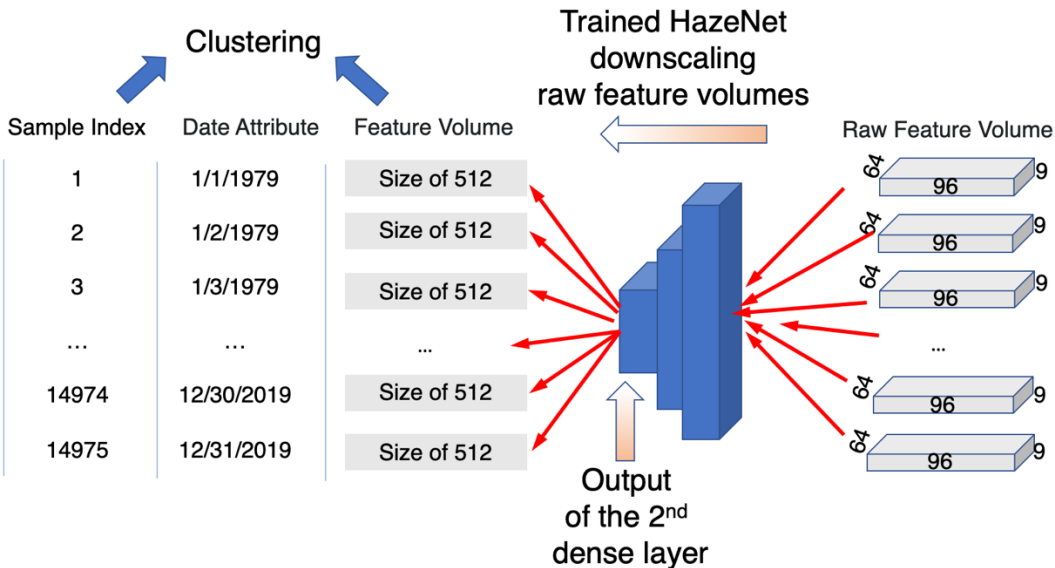
Figure 6. A diagram of the cluster analysis procedure. Here 96, 64, and 9 represent the number of longitudinal, latitudinal grids, and number of features (variables), or the size of the input feature volume of a trained HazeNet for Beijing cases, while 512 is the size of the output from the dense layer before output layer of HazeNet or the new feature volume.

In order to provide useful information for understanding the performance of the trained networks, the clustering has been performed for each of the prediction outcomes rather than just haze versus non-haze events (Appendix C). In this configuration, haze associated regimes are represented by derived clusters of TP plus FN outcomes, while non-haze regimes by those of TN plus FP. Since the clusters were derived using the indices of samples as the record for members, the actual feature maps of the members in any cluster thus can be conveniently retrieved then used to identify the representative regimes in terms of combined 9 meteorological and hydrological features. Here the clustering results have been analyzed using the feature maps in both normalized (machine native) and unnormalized (original reanalysis data) format. The characteristics of various regimes can be easily identified from the former as they represent anomalies to climatological means. An added benefit is to advance the understanding of the performance of the trained networks. The analysis using the latter maps aims to better appreciate the conventional regional and local meteorological and hydrological patterns associated with various regimes. The feature maps used in both analyses have been averaged across each cluster for clarity.

4.1 Results based on normalized feature maps

As shown in Figure 7, the 4 clusters of true positive or TP in Beijing cases exhibit a clear similarity in general feature patterns closely surrounding Beijing (marked by a navy dot in the figure) among themselves. These common patterns include an isolated small positive relative humidity (REL) center covering Beijing, associated with mild diurnal variation change (DT2M) and standard deviation (T2MS) of surface temperature as well as zonal wind (U10), and a lower boundary layer height (BLH). Weatherwise, Beijing and its immediate surrounding area appear to be located between two sharply different airmasses occupying respectively the northwestern and southeastern part of the domain (weather systems usually progress from northwest to

southeast in this region). When relating this to the other feature characteristics, it is likely that Beijing and nearby area is not experiencing a drastic weather system change such as fronts when haze occurs, hence the high REL- a critical condition for aerosol to effectively scatter sunlight - can be easily formed, aided by a stable boundary layer with mild surface wind to allow aerosols well mix vertically near the ground while without being significantly reduced through advection diffusion. In addition, relatively high soil water content could fuel the humidity in the air, and thin while stable low clouds, if exists (judged based on temperature change) could signal a lack of persistent precipitation. Altogether, these conditions can apparently allow the haze to easily form, to last, and to effectively scatter sunlight thus reduce visibility. These conditions are also in a noticeably contrast to those associated with non-haze events represented by TN outcomes (Fig. S4).

Note that each cluster consists of a collection of 3D data volumes or images, any two clusters could be sufficiently differentiated should only one of their images differs based on the clustering derivation algorithm, even though statistically speaking, they very likely belong to the same population (*i.e.*, should be tested statistically). As shown in Fig. 7, the distinctions between TP clusters are largely reflected from the two different airmasses distant from Beijing, in both strength and spatial extent particularly from DTCV patterns, likely representing different types of systems or background regimes. Specifically, a strong DTCV anomalous center seen in cluster 1 and 4 patterns occupies most of the domain west of Beijing and directly influence Beijing and its nearby area. In contrast, DTCV distributions in cluster 2 and 3 are much weaker, where Beijing and its immediate neighboring area even appear to be influence more by the southeaster system. In addition, surface wind distributions of the first two clusters clearly differ from those of cluster 3 and 4, and the patterns of BLH alongside SW1 and SW2 over Beijing and its immediate neighboring area of cluster3 also suggests a land-atmosphere exchange condition differing from that of others. The combinations of these differences across various TP clusters apparently well defines the various regimes of surrounding weather systems as well as their influence on Beijing. For TP clusters of Shanghai, the above similarities alongside differences among various clusters also exist, except where the cluster 1, 2, and 4 maintain more similarities in feature patterns of distant airmasses from Shanghai, while cluster 3 offers certain evident diversity in many feature patterns comparing to other clusters (Fig. S5). Even more interestingly, the distribution of the number of members within various TP clusters does not differ evidently in different months (Table S1) (note that the number of haze events itself differs seasonally – Fig. 5). Therefore, it is very likely that the characteristic weather conditions favoring haze occurrence and being captured by HazeNet cannot be simply differentiated by locations (Beijing vs. Shanghai) and seasons.

On the other hand, among three FN clusters (also associated with haze events but missed in prediction), only the first cluster (the major cluster of FN) displays a clearcertain similarity to TP clusters across most various features, though. Even for this cluster, the characters of the airmasses distantly surrounding Beijing differ substantially from those of TP clusters, as seen from the patterns of temperature (DT2M, T2SM), wind particularly V10, and column water (DTCV) that reflect a much weaker weather system on the west. The patterns of BLH, SW1, and SW2 also differ from those of TP, indicating a different near site boundary layer and hydrological condition. Such differences appear to be even more evidently in the two other (minor) clusters alongside some of the common features in TP clusters, *e.g.*, the size and strength of high relative humidity center covering Beijing are even different. This result suggests a possible reason for why HazeNet missed these targets, that is haze might occur under

439 unfavorable weather and hydrological conditions owing to, *e.g.*, certain energy consumption
440 scenarios. Again, the distribution of members of these latter two clusters does not exhibit clear
441 seasonality (Table S1). Interestingly, first two of the four FP (false alarm) clusters display more
442 clear similarity in normalized feature patterns to those of TP than FN in Beijing and its
443 immediate surrounding area (Fig. 7). As in FN cases, however, two other clusters differ more
444 evidently. All these could explain the false alarming made by the machine, *i.e.*, the machine
445 could have simply been confused by such similarities between certain TP and FP members.
446 Nevertheless, these could also suggest an alternative reason behind the incorrect forecasts that is
447 certain pollution mitigation measures were in place. The results of FP clusters and the last FN
448 cluster besides TP of Shanghai cases also share some similar characters as analyzed here (Fig S5
449 & S6).
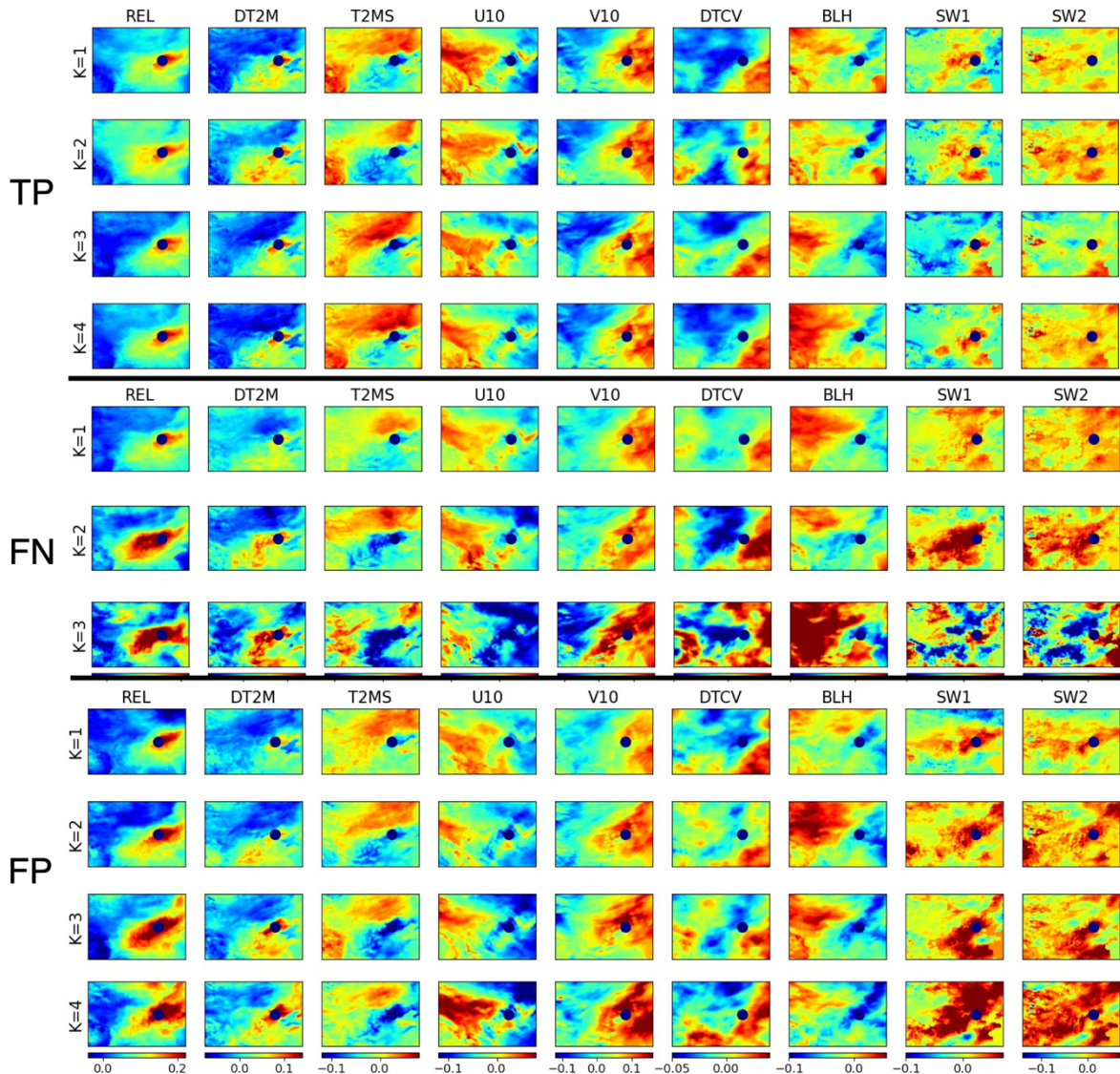
450
451 **Figure 7**. Maps of 9 features in normalized format for 4 clusters of true positive or TP outcome, 3 clusters
452 of false negative or FN outcome, and 4 clusters of false positive or FP outcome. Here TP plus FN = haze
453 events. Results shown are cluster averages for Beijing (location marked by navy dot) cases.

454   Therefore, it is worth indicating again that meteorological or hydrological conditions are not
455 the only factors determining the occurrence of hazes. Other factors such as abnormal energy
456 consumption events or long-range transport of aerosols could all cause haze to occur even under
457 unfavorable weather and hydrological conditions. This could well be the reason for some of the
458 missing forecasts (FN outcomes) when haze occurred under unfavorable conditions, as suggested
459 above, or for false alarms (FP outcomes) when low aerosol events occurred even under a weather
460 condition favorable to haze. Future improvement of the skill could benefit from this knowledge.

4.2 Results based on original unnormalized feature maps

462   Utilizing feature maps in their original unnormalized format represented by actual physical
463 quantities could provide a convenience to appreciate the conventional regional and local
464 meteorological and hydrological patterns ~~associated with various events~~, and to detect thus to
465 implement additional analysis, if necessary, on the possible impact of seasonality or trend
466 associated with various events. Note that the visual differences between unnormalized feature
467 maps particularly in cluster-mean format might be subtle for bare eyes to recognize.
468   For haze events in Beijing (*i.e.*, TP and FN outcomes; Fig. 8), the associated cluster-mean
469 regional meteorological and hydrological patterns of most features except DTCV contain two
470 regions with sharply contrasting quantities, roughly separated by a line linking the southwest and
471 northeast corner of the domain, likely due to the typical progression direction of weather systems
472 in this region besides meridional variation of general climate. In comparison, as same as shown
473 in the previous analysis using normalized feature maps, the patterns of the first FN cluster share
474 many characters with those of TP clusters. The differences among TP and FN clusters are more
475 evident in DTCV (specifically cluster 1 and 4 versus cluster 2 and 3), SW1, SW2, and surface
476 winds particularly for the 2nd and 3rd FN clusters. FP clusters also display a similarity to those of
477 TP clusters (Fig. S7), whereas TN clusters show more visible differences particularly in patterns
478 of meridional wind (V10) and daily change of column water vapor or DTCV (Fig. S8).

479
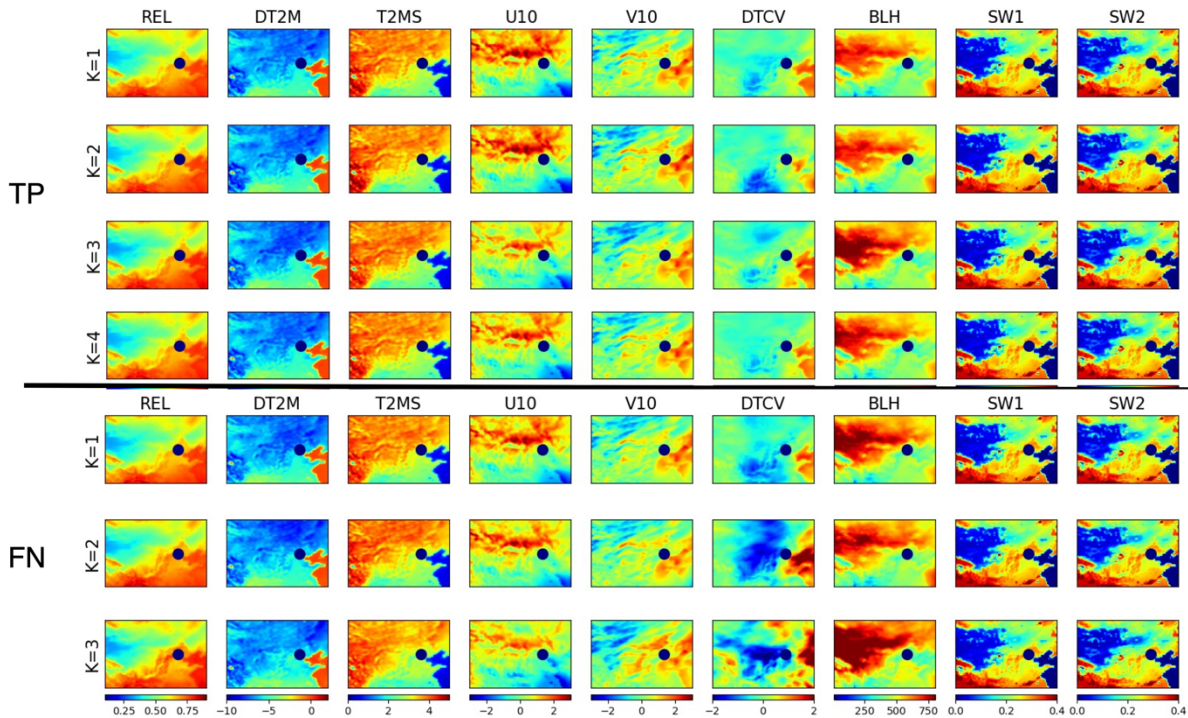
Figure 8. Feature maps associated with severe haze events in Beijing represented by 4 clusters of TP (4 top rows) and 3 clusters of FN (3 lower rows) predicted outcomes. Shown are cluster means of unnormalized data of relative humidity or REL (ratio), diurnal change (DT2M) and daily standard deviation (T2MS) of 2-meter temperature in degree, 10-meter winds U10 and V10 in m/s, diurnal change of column water vapor or DTCV (kg/m^2), planetary boundary hheight ot BLH in meter, and soil water content in soil level 1 (SW1) and level 2 (SW2) in kg/m^2.

The general regional meteorological and hydrological conditions during haze events in the southeastern in comparison to the northwestern portion of the domain include a higher relative humidity, lower variation of surface temperature, largely northward or northwestward wind, lower planetary boundary layer height, and higher soil water content, and quantity wise these are all in a sharp contrast to the situations in the other half of the domain. Based on the surface wind direction, Beijing and its immediate surrounding area is clearly located between two airmasses both with anticyclonic surface winds. The strengths of these two centers differ particularly in the last two FN clusters, implying regimes with systems having different strengths or in different development phases. Such a difference is also clearly related to the visually recognized cross-cluster difference in DTCV patterns, represented by a strong negative center in the middle of the domain with varying extent and strength across different clusters. Consistent to the analysis result using normalized feature maps, all these indicate a stable weather condition over Beijing and its neighboring area during haze events while surrounded by two (or more) different weather systems. It is known that dust can cause low visibility events in Beijing. During dust seasons, the condition of the northwestern half of the domain, represented by a dominant eastward wind and lower soil water content likely favors dust transport from desert to Beijing. However, the details would need an in-depth analysis to examine since most clusters having members rather well distributed through different months (Table S1).

The cluster-means of 9 features for haze events (TP plus FN) versus non-haze (TN plus FP) at the grid point of Beijing are also derived and listed in Table 1 for reference. Specifically, the common local conditions associated with hazes in Beijing in comparison to those with non-haze events include a higher humidity, less drastic variations in surface temperature, a northwestward rather than southeastward wind, a lower planetary boundary layer height, and higher soil water contents. Again, the most recognizable cross-cluster differences appear in DTCV (*i.e.*, cluster 1 versus others), followed by surface wind (cluster 1 and 2 versus 3 and 4). In most of the local features, variabilities of FN clusters tend to be larger than those of TP clusters. Notably, such differences in local feature quantities for FN clusters are not necessarily more evident than in the regional maps over distant airmasses. One interesting result of the local weather conditions shown in Table 1 is that the cluster means of TN are sharply different than those of TP and FN, while the cluster means of FP and those of TP+FN are likely to be statistically indifferent except for DTCV, providing an evidence to support the assumption that FP outcomes might simply represent the non-haze events caused by reasons other than weather and hydrological conditions.

For the case of Shanghai, the general weather conditions associated with haze events are likely stable, with characters similar to the cases of Beijing except for that Shanghai appears to be located between a northwest airmass with anticyclonic surface wind and a southeast one with cyclonic wind (Fig. 9). Quantities of most feature patterns display a sharply southeast versus northwest contrast. DTCV maps display a negative center over a large area, its distribution and extent vary significantly among different clusters in particular for the first two FN clusters. The patterns of soil water content in both soil layers exhibit a sharp meridional contrast, much higher in the south part of the domain than in the north part, largely separated by the Yellow River. Local quantities of all the features associated with haze events (TP plus FN) in Shanghai display

clear differences with those of non-haze prediction outcomes (TN) (Table 1). The most
recognizable cross-cluster differences for TP appear in U10 of cluster 4 and V10 of cluster 3,
differing from the cases of Beijing, and DTCV particularly of cluster 3 for FN. Like the cases of
Beijing, the cluster mean of the FP outcomes is statistically indifferent to those of haze (TP and
FN) than predicted non-haze (TN) events. Again, this result implies that even a weather pattern
favoring haze appeared and was correctly recognized by HazeNet, due to other factors such as
energy consumption variations, haze could still not to occur.
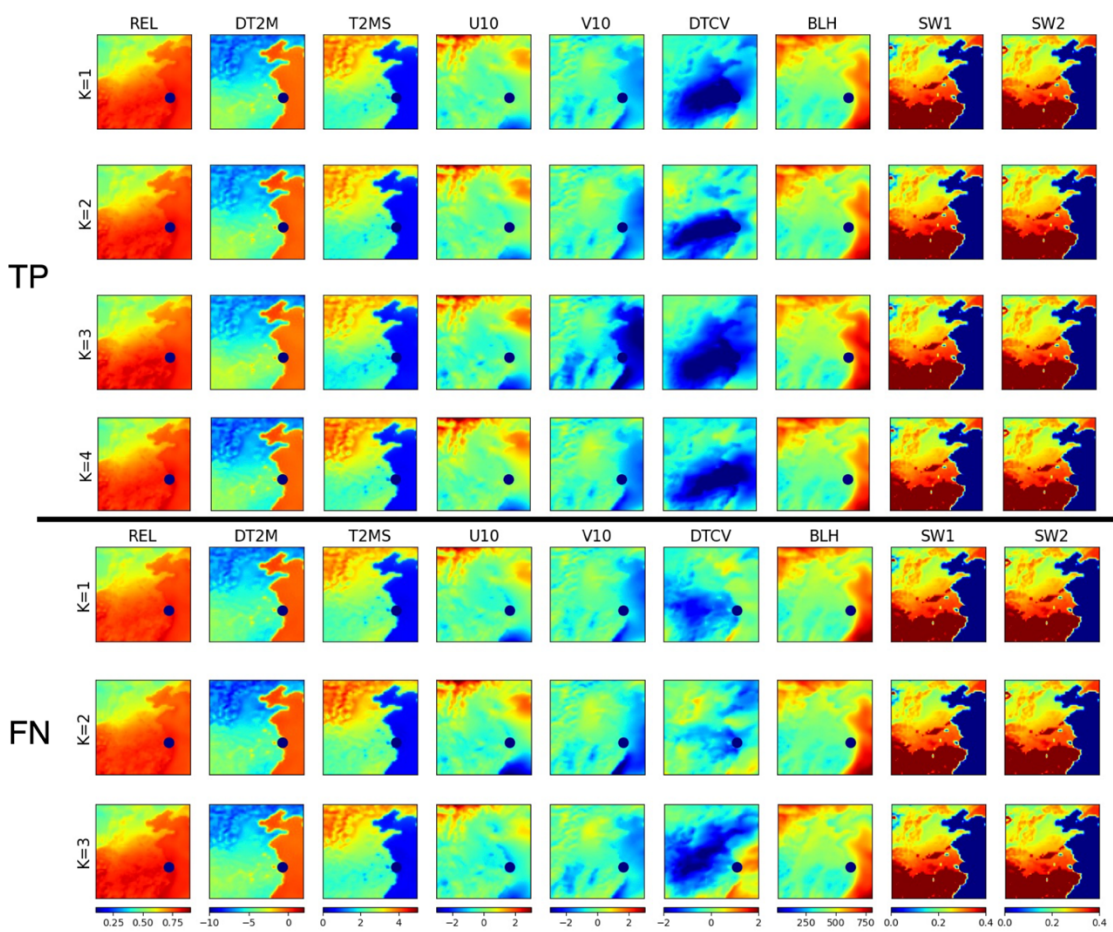
Figure 9. The same as Figure 9 except for Shanghai with 4 clusters for TP and 3 for FN outcomes.

It is worth indicating that the current analysis discussed here is only applied to the included
features in clustering, and the presented figures in cluster-wise averaging format might have
effectively smoothed out certain variability among members. A full-scale analysis would
necessarily go beyond this to provide further synoptical or large-scale hydrological insights and
better define different regimes.

Table 1. Cluster means of features associated with haze events (TP and FN) in Beijing and Shanghai versus means of all clusters of non-haze events of TN and FP, respectively. Number of cluster members of each cluster are listed in bracket.

Cluster	REL (0-1)	DT2 (ºC)	T2MS (ºC)	U10 (m/s)	V10 (m/s)	DTCV (kg/m²)	BLH (m)	SW1 (kg/m²)	SW2 (kg/m²)
Beijing									
TP1 (848)	0.64	-5.99	3.24	-0.29	0.20	0.04	379.71	0.23	0.22
TP2 (181)	0.65	-5.80	3.14	-0.28	0.19	0.57	378.33	0.23	0.23
TP3 (354)	0.65	-5.39	2.98	-0.45	0.29	0.31	400.20	0.23	0.22
TP4 (1208)	0.64	-5.82	3.18	-0.34	0.28	0.27	381.28	0.23	0.22
FN1 (392)	0.63	-6.24	3.32	-0.25	0.20	0.07	422.60	0.23	0.22
FN2 (90)	0.65	-5.71	3.05	-0.20	0.17	0.19	406.65	0.23	0.22
FN3 (26)	0.69	-5.37	2.94	-0.61	0.39	-0.17	410.95	0.25	0.23
TN mean	0.51	-7.13	3.65	0.15	-0.15	0.36	552.90	0.22	0.21
FP mean	0.65	-5.84	3.15	-0.35	0.25	-0.26	386.27	0.24	0.23
Shanghai									
TP1 (1228)	0.81	-3.44	1.79	-0.16	-0.55	-2.25	415.59	0.35	0.35
TP2 (135)	0.81	-3.10	1.71	-0.12	-0.66	-2.08	422.04	0.36	0.36
TP3 (689)	0.81	-2.95	1.59	-0.17	-1.28	-2.29	472.74	0.36	0.35
TP4 (355)	0.81	-3.52	1.82	0.03	-0.57	-2.74	411.96	0.35	0.35
FN1 (372)	0.80	-3.48	1.80	-0.41	-0.42	-0.84	421.13	0.35	0.35
FN2 (113)	0.80	-3.64	1.84	-0.34	-0.51	-1.21	423.09	0.35	0.34
FN3 (107)	0.82	-3.28	1.77	-0.68	-0.49	0.10	422.36	0.35	0.35
TN mean	0.77	-3.29	1.57	-2.86	1.40	0.62	739.75	0.31	0.32
FP mean	0.82	-3.26	1.71	-0.48	-0.85	-2.26	438.55	0.35	0.35

5 Summary and Conclusions

Following an earlier preliminary attempt for hazes in Singapore, a deep convolutional neural network containing more than 20 million parameters, namely HazeNet, has been further developed to test forecasting the occurrence of severe haze events during 1979-2019 in two metropolitans of Asia, Beijing and Shanghai. By training the machine to recognize regional patterns of meteorological and hydrological features associated with haze events, the study would advance our knowledge about this still poorly known environmental extreme. The deep CNN has been trained in a supervised learning procedure using the time sequential maps of up to 16 meteorological and hydrological variables or features as inputs and surface visibility observations as the labels.

562 Even with a rather limited samples (14,975), the trained machine has displayed a reasonable
563 performance measured by commonly adopted validation metrics. Its performance is clearly better
564 during months with high haze frequency, *i.e.*, all months except dusty April and May in Beijing
565 and from late autumn through entire winter in Shanghai. Relatively larger spatial patterns appear
566 to be more effective than the smaller ones to influence the performance of forecasting. On the
567 other hand, in-depth analysis on performance results has also indicated certain limitations of
568 current approach of solely using meteorological and hydrological data in performing forecast.
569 The trained machine has also been used to examine the sensitivity of the CNN to various
570 input features and thus to identify then remove features ineffective to the performance of the
571 machine. In addition, to further categorize typical regional weather and hydrological patterns
572 associated with severe haze versus non-haze events, an unsupervised cluster analysis has been
573 subsequently conducted, benefited from using features with greatly reduced dimensionality
574 produced by the trained machine.
575 The cluster analysis has, arguably for the first time, successfully categorized major regional
576 meteorological and hydrological patterns associated with severe haze and non-haze events in
577 Beijing and Shanghai into a limited number of representative groups, with the typical feature
578 patterns of these clustered groups derived. It has been found that the typical weather and
579 hydrological regimes of haze events in Beijing and Shanghai are rather stable conditions,
580 represented by anomalously high relative humidity, low planetary boundary layer height, mild
581 daily temperature change that likely associated with a thin low cloud cover over the haze
582 occurring regions. The result has further revealed a rather strong similarities in
583 associated meteorological and hydrological regimes between haze
584 and false alarm clusters, or differences between haze and missing forecasting
585 clusters, implying that factors
586 such as energy consumption variations, long range transport of aerosols,
587 or beyond, could influence the occurrence of hazes   even under unfavorite
588 weather conditions.
589 Due to the exploratory nature of this specific effort, several aspects could be further
590 optimized including the rather arbitrary though statistically meaningful labeling. Also, an in-
591 depth analysis on weather regimes would necessarily involve the use of certain features that are
592 not included in the current clustering, which, however, exceeds the extent of this paper and can
593 only be discussed properly in a future work. Nevertheless, this study has demonstrated the
594 potential of applying deep CNNs with extensive multi-dimensional and time sequential
595 environmental images to advance our understandings about poorly known environmental and
596 weather extremes. The methodology, results alongside experience obtained from this study could
597 benefit future improvement of the skills. Besides, the trained machines can be used in many
598 other types of machine learning and deep learning applications as partially demonstrated here.

599 Appendix A. Performance metrics

600 Several commonly used performance metrics have been used in this study. They are largely derived based on
601 the so-called confusion matrix (e.g., Swets, 1988) as defined in the following Table A.
602
603 **Table A**. Confusion matrix for measuring the prediction outcomes of a given class.

	Observed	
	Positive	*Negative*

Predicted	Positive	True Positive or TP	False Positive or FP
	Negative	False Negative or FN	True Negative or TN

604 Here, *positive* or *negative* is referring to the outcome of a given event or class in the classification, *e.g.*, severe haze
605 or non-haze events. Hence, the prediction outcome TP is a correct forecast of a severe haze while TN a correct
606 forecast of a non-haze event, FP represents a false alarm, and FN a missing forecast. The context of outcomes
607 changes when the designated class is switched. The major performance metrics used in this paper include:

608 $$accuracy = \frac{TP+TN}{N} \qquad \text{(A1)}$$

609 $$precision = \frac{TP}{TP+FP} \qquad \text{(A2)}$$

610 $$recall = \frac{TP}{TP+FN} \qquad \text{(A3)}$$

611 $$F1\ score = 2 \cdot \frac{precision \cdot recall}{precision+recall} \qquad \text{(A4)}$$

612 $$ETS = \frac{TP-Hit_{random}}{TP+FP+FN-Hit_{random}} ; \qquad \text{(A5a)}$$

613 $$\text{where:} \quad Hit_{random} = \frac{(TP+FN) \cdot (TP+FP)}{N} \qquad \text{(A5b)}$$

614 $$HSS = \frac{2 \cdot (TP \cdot TN - FP \cdot FN)}{(TP+FP) \cdot (FP+TN) + (TP+FN) \cdot (TP+TN)} \qquad \text{(A6)}$$

615 Note that *accuracy* has the same value for all the classes and thus is a good metrics for the overall classification.
616 Values of all the other metrics differ depending on the referred specific class. Here, *F1 score* is the F-score with $\beta =$
617 1 (van Rijsbergen, 1974), *ETS* represents equitable threat score (or Gilbert skill score; Gilbert, 1884; range = [-1/3,
618 1]), *HSS* represents Heidke skill score (Heidke, 1926; range = [-∞,1]), and *N* is the number of total outcomes.

619 **Appendix B. Examining the network's sensitivity to features using trained machine**

620 A method has been adopted in this study to use a trained machine from basic training to examine the sensitivity
621 of the network to a random perturbation applied to the values of different features. The saved machine contains all
622 the coefficients in different network layers and can be used to predict output from any of these layers using same
623 input features for training or validation. The sensitivity of the network to a given feature is determined by comparing
624 the prediction using input feature maps containing randomly perturbation applied to the map of this feature with the
625 prediction using original input feature maps, and measured by the content loss between these two predictions, with
626 *img1* with *MxN* pixels as the unperturbed and *img2* as perturbed network output:

627 $$Content\ Loss = \frac{1}{M \times N} \sum_{i,j}^{M,N} (img1_{i,j} - img2_{i,j})^2 \qquad \text{(B1)}$$

628 The perturbation is applied as random patch with addition of -0.2 or 0.2 to 10% of the pixels of the input map of
629 the targeted feature in each sample while maps of all the other features remain unperturbed. To reduce the workload,
630 only validation input set corresponding to the class 1 events (about 1020 samples) are used. Therefore, the
631 sensitivity tested here is actually the sensitivity of the network to a given feature in predicting class 1 events. To
632 preserve the spatial information of the perturbation field, the output of the 9th layer, or the MaxPooling layer
633 following the second convolutional layer (Fig. 1) is used as the prediction. It has a size of (15, 31, 92) for Beijing
634 cases and (15, 15, 92) for Shanghai cases when a kernel size of 20x20 is adopted. A higher content loss represents
635 that the performance of the network is more sensitive to the variations in value of this feature.

636 **Appendix C. Cluster analysis**

637 The cluster analysis of this study was conducted in the following three steps (see also Fig. 6).
638 **(i)** Firstly, the trained and saved HazeNet for both Beijing and Shanghai cases with 9 input features have been
639 used to perform prediction using the entire 14,975 input samples in original raw data format, *i.e.*, with a feature
640 volume size of 96x64x9 for Beijing and 64x64x9 for Shanghai for each sample. The prediction results were then
641 summarized into various outcomes, *e.g.,* as true positive (TP), true negative (TN), false positive (FP), or false

negative (FN) in referring to the haze class. In the meantime, the output of the second dense layer just before the output layer or latent space (see Fig. 1 & Fig. 6) were further used to form the new data of each sample with reduced feature volume of 512. This new dataset with 14075 samples and 512 feature volume were ready for clustering.

(ii) The second step is to actually perform clustering using the new data with reduced size resulted from the previous step. For this purpose, it should be conducted separately for different types of samples or events, *e.g.*, categorizing all the samples for haze into characteristic groups with similarity and same for non-haze events. In order to provide additional information to further the understanding of the network's performance, the clustering was actually conducted for different prediction outcomes, by taking corresponding samples from the new dataset. In this case, TP plus FN would lead to haze events, and TN plus FP to non-haze events. The clustering calculations were done by directly using the k-mean (Steinhaus, 1957) function of scikit-learn library (https://scikit-learn.org/stable/modules/clustering.html#clustering). For Beijing cases, the trained machine with 9 features produced 2591 TP, 11368 TN, 508 FP, and 508 FN outcomes, and 2407 TP, 11484 TN, 492 FP, and 592 FN for Shanghai. The cluster analysis was performed separately for each of these outcomes in an unsupervised learning procedure to let the machine to categorize corresponding samples into groups based on similarities among them. In practice, similarity is judged by the so-called inertia for a cluster with members of x_i and mean of μ:

$$inertia = \sum_i^N(\|x_i - \mu\|)^2 \qquad (C1)$$

The clustering is to seek a grouping with minimized inertia within each cluster. The overall measure is the summation inertia that decreases almost exponentially with the increase of number of clusters. In practice, the cluster analysis was first tested with various given number of clusters ranging from 1 to 100, to examine the values alongside decay of the inertia. This provided a base to identify the smallest possible number of cluster centers with reasonably low inertia in actual cluster analysis. This has actually been decided by using square root of the inertia weighted by the number of samples to put the varying number of samples across various outcomes in consideration. An optimized number of clusters was chosen with a weighted inertia lower than 1/e of that of the single cluster case. For TN, due to the large sample number, this criterion was set to be half of 1/e. As a result, the optimized numbers of clusters for TP, FN, FP, and TN outcomes are 4, 3, 4, and 15 for Beijing and 4, 3 3, and 10 for Shanghai, respectively,

(iii) The members of each cluster derived from (ii) were recorded by the actual sample indices with date attribute. Therefore, actual samples of input data grouped into various clusters can be thus conveniently identified with corresponding feature maps retrieved, either in the format of normalized or unnormalized (*i.e.*, in original quantity as in reanalysis dataset), and used for further analyses. In practice, cluster-averaged maps for various features were performed beforehand.

Code and data availability

The Python script for network architecture, training and validation is rather straightforward and simple, basically consisting of directly adopted function calls from Keras interface library (https://github.com/keras-team/keras) with TensorFlow-GPU (https://www.tensorflow.org) as backend, or from scikit learn library (https://scikit-learn.org/). All the data used for analyses are publicly available as indicated in the Acknowledgements.

Competing interests

The author declares that he has no conflict of interest.

Acknowledgements

This study is supported by L'Agence National de la Recherche (ANR) of France under "Programme d'Investissements d'Avenir" (ANR-18-MPGA-003 EUROACE). The author thanks the European Centre for Medium-range Weather Forecasts for making the ERA5 data publicly available under a license generated and a service offered by the Copernicus Climate Change Service, and the National Center for Environmental Information of the US NOAA for making GSOD data available. All the related computations have been accomplished using the GPU clusters of French Grand equipment national de calcul intensif (GENCI) (Project 101056) and the CNRS

688 Mesocenter of Computing of CALMIP (Project p18025). Constructive comments and suggestions from two
689 anonymous reviewers have led to the improvement of the manuscript.

690 **References**

691 Chan, C. K. and Yao, X.: Air pollution in mega cities in China, Atmos. Environ., 42, 1-42, 2008.
692 Chattopadhyay, A., Nabizadeh, E. and Hassanzadeh, P.: Analog forecasting of extreme-causing
693   weather patterns using deep learning. *J. Adv. Modeling Earth Sys.*, 12, e2019MS001958.
694   Doi:/10.1029/2019MS001958, 2020.
695 Forest, D.: *Generative Deep Learning*, O'Reilly Media, Inc., 2019.
696 Gagne, D., Haupt, S. and Nychka, D.: Interpretable deep learning for spatial analysis of severe
697   hailstorms. *Mon. Wea. Rev.*, 147, 2827–2845, Doi:/10.1175/MWR-D-18-0316.1, 2019.
698 Gilbert, G. K.: Finley's tornado predictions, *Amer. Meteor. J.*, 1, 166–172, 1884.
699 Goodfellow, I., Bengio, Y. and Courville, A.: *Deep Learning*, MIT Press, 800pp., 2017.
700 Grover, A. Kapoor, A. and Horvitz, E.: A deep hybrid model for weather forecasting, *Proc. 21st
701   ACM SIGKDD Intern'l Conf. KDD*, p.379-386, Sydney, Australia, August 10, 2015. ACM.
702   ISBN 978-1-4503-3664-2/15/08. Doi:10.1145/2783258.2783275, 2016.
703 He, K., Zhang, X., Ren, S. and Sun, J.: Deep residual learning for image recognition,
704   arXiv:1512.03385, 2015.
705 Heidke, P.: Calculation of the success and goodness of strong wind forecasts in the storm
706   warning service, *Geogr. Ann. Stockholm*, 8, 301–349, 1926.
707 Hersbach, H., Bell, B., Berrisford, P., Hirahara, S., Horányi, A., Muñoz-Sabater, J., Nicolas, J.,
708   Peubey, C., Radu, R., Schepers, D., Simmons, A., Soci, C., Abdalla, S., Abellan, X.,
709   Balsamo, G., Bechtold, P., Biavati, G., Bidlot, J., Bonavita, M., De Chiara, G., Dahlgren, P.,
710   Dee, D., Diamantakis, M., Dragani, R., Flemming, J., Forbes, R., Fuentes, M., Geer, A.,
711   Haimberger, L., Healy, S., Hogan, R. J., Hólm, E., Janisková, M., Keeley, S., Laloyaux, P.,
712   Lopez, P., Lupu, C., Radnoti, G., de Rosnay, P., Rozum, I., Vamborg, F., Villaume, S. and
713   Thépaut, J.-N.: The ERA5 global reanalysis, *Q. J. R. Meteorol. Soc.*, 146, 1999-2049, 2020.
714 Ioffe, S. and Szegedy, C.: Batch normalization: Accelerating deep network training by reducing
715   internal covariate shift, arXiv:1502.03167, 2015.
716 Jiang, G.-Q., Xu, J. and Wei, J.: A deep learning algorithm of neural network for the
717   parameterization o typhoon-ocean feedback in typhoon forecast models, *Geophys. Res. Lett.*,
718   45, https://doi.org/10.1002/2018GL077004, 2018.
719 Kiehl, J. T. and Briegleb, B. P.: The relative roles of sulfate aerosols and greenhouse gases in
720   climate forcing, *Science*, 260, 311-314, 1993.
721 Kurth, T., Treichler, S., Romero, J., Mudigonda, M., Luehr, N., Phillips, E., Mahesh, A.,
722   Matheson, M., Deslippe, J., Fatica, M., Prabhat and Houston, M.: Exascale deep learning for
723   climate analytics, arXiv:1810.01993, 2018.
724 Lagerquist, R., McGovern, A. and Gagne II, D.: Deep learning for spatially explicit prediction of
725   synoptic-scale fronts. *Wea. Forecasting*, 34, 1137–1160. Doi:10.1175/WAF-D-18-0183.1,
726   2019.
727 LeCun, Y., Bengio, Y. and Hinton, G.: Depp learning, *Nature*, 521, 436-444,
728   doi:10.1038/nature14539, 2015.
729 Lee, H.-H., Iraqui, O. and Wang, C.: The impacts of future fuel consumption on regional air
730   quality in Southeast Asia, *Sci. Rep.*, 9:2648, doi:10.1038/s41598-019-39131-3, 2019.
731 Lee, H.-H., Iraqui, O., Gu, Y., Yim, H.-L. S., Chulakadabba. A., Tonks, A. Y. M., Yang, Z. and
732   Wang, C.: Impacts of air pollutants from fire and non-fire emissions on the regional air

quality in Southeast Asia, *Atmos. Chem. Phys.*, 18, 6141–6156, doi:10.5194/acp-18-6141-2018, 2018.

Lee, H.-H., Bar-Or, R. and Wang, C.: Biomass Burning Aerosols and the Low Visibility Events in Southeast Asia, *Atmos. Chem. Phys.*, 17, 965-980, doi:10.5194/acp-17-965-2017, 2017.

Lin, Y., Wijedasa, L. S. and Chisholm, R. A.: Singapore's willingness to pay for mitigation of transboundary forest-fire haze from Indonesia, *Environ. Res. Lett.*, 12, 024017, doi:10.1088/1748-9326/aa5cf6, 2016.

Liu, M., Huang, Y., Ma, Z., Jin, Z., Liu, X., Wang, H., Liu, Y., Wang, J., Jantunen, M., Bi, J. and Kinney, P. L.: Spatial and temporal trends in the mortality burden of air pollution in China: 2004-2012, Environ. Int., 98, 75-81, 2017.

Liu, Y., Racah, E., Prabhat, Correa, J., Khosrowshahi, A., Lavers, D., Kunkel, K., Wehner, M. and Collins, W.: Application of deep convolutional neural networks for detecting extreme weather in climate datasets. arXiv:1605.01156, 2016.

McGovern, A., Lagerquist, R., Gagne II, D. J., Jergensen, G. E., ElmLMore, K. L., Homeyer, C. R. and Smith, T.: Making the black box more transparent: Understanding the physical implications of machine learning, *Bull. Amer. Meteor. Soc.*, 100, 2175-2199, 2019.

Ronneberger, O., Fischer, P. and Brox, T.: U-Net: Convolutional networks for biomedical image segmentation, arXiv:1505.04597, 2015.

Shi, X., Chen, Z., Wang, H. and Yeung, D.-Y.: Convolutional LSTM network: A machine learning approach for precipitation nowcasting, arXiv:1506.04214, 2015.

Silva, R. A., West, J. J., Zhang, Y., Anenberg, S. C., Lamarque, J.-F., Shindell, D. T., Collins, W. J., Dalsoren, S., Faluvegi, G., Folberth, G., Horowitz, L. W., Nagashima, T., Naik, V., Rumbold, S., Skeie, R., Sudo, K., Takemura, T., Bergmann, D., Cameron-Smith, P., Cionni, I., Doherty, R. M., Eyring, V., Josse, B., MacKenzie, I. A., Plummer, D., Righi, M., Stevenson, D. S., Strode, S. Szopa, S. and Zeng, G.: Global premature mortality due to anthropogenic outdoor air pollution and the contribution of past climate change, *Environ. Res. Lett.*, 8, 034005, doi:10.1088/1748-9326/8/3/034005, 2013.

Simonyan, K. and Zisserman, A.: Very deep convolutional networks for large-scale image recognition, arXiv:1409.1556, 2015.

Smith, A., Lott, N. and Vose, R.: The integrated surface database: Recent developments and partnerships, *Bull. Ameri. Meteorol. Soc.*, 92, 704-708, doi:10.1175/2011BAMS3015.1, 2011.

Steinhaus, H.: Sur la division des corps matériels en parties, *Bull. Acad. Polon. Sci.*, 4, 801–804, 1957.

Swets, J.: Measuring the accuracy of diagnostic systems, *Science*, 240, 1285–1293, 1988.

Szegedy, C., Vanhoucke, V., Ioffe, S., Shlens, J. and Wojna, Z.: Rethinking the inception architecture for computer vision, arXiv:1512.00567, 2015.

van Rijsbergen, C., 1974: Foundation of evaluation, *J. Documentation*, 30, 365–373.

Wang, C.: Exploiting deep learning in forecasting the occurrence of severe haze in Southeast Asia, arXiv:2003.05763, 2020.

Weyn, J. A., Durran, D. R. and Caruana, R.: Improving data-driven global weather prediction using deep convolutional neural networks on a cubed sphere, *J. Adv. Modeling Earth Sys.*, e2020MS002109, https://doi.org/10.1029/2020MS002109, 2020.